# Design of Wide Angle and Large Aperture Optical System of a Lidar Sensor for Characterization of Space Debris Particles

**Davud Asemani, George Rossano, John McVey, Shawn Perdue, Joel Rivera, Matthew Kelley, Henry Helvajian, and Marlon Sorge**

*The Aerospace Corporation, 2310 E. El Segundo Blvd El Segundo CA 90245 USA*

**Abstract**

Millions of debris pieces are currently in Earth orbit. The debris objects depending on their sizes can pose either mission termination risks (larger than ~5 mm) or mission degradation risks (smaller than 1 mm). However, the current sub-mm debris environment has not been characterized well because of the limited availability of measurements. We have designed a special Light Detection and Ranging (Lidar) as a novel approach to the detection and characterization of sub-mm space debris objects for in situ, and non-contact measurement. The desired Lidar design is constrained in size and power and meant to be flown aboard a 6U CubeSat. It provides a detection area that is one order of magnitude larger than the current state-of-the-art which is a one square meter impact detector. The debris-sensor incorporates a pulsed laser and generates an optical fan-shaped beam. Given the nature of the pulse, and the operational duty cycle, the Lidar is designed to detect small debris passing through the laser net. The design is based on commercial-off-the-shelf lasers, detectors, and filters and meets the technical specifications and mission requirements for a small debris detection system that is intended to operate in low earth orbit (LEO).

In this paper, we present the design of the receiver optical system. The illuminated volume consists of a rectangular region bounded by wide angle (50 degrees) on one axis and a narrow angle (6 degrees) in the orthogonal axis and a range spanning to 20 meters. Our design uses Photo-Multiplier Tubes (PMT) to acquire both high gain (e.g., $10^6$) and fast response (e.g., ns) in comparison to CCD or CMOS detectors which must acquire photons, store charge, to realize gain. Three PMTs, each with an effective area of 14x14mm, are used as the detector system. The collecting lens, constrained by the 6U CubeSat structure, has a 90 mm diameter aperture and 144 mm focal length. While PMTs have advantages over solid state detectors, one disadvantage is that the PMT photo cathode sensitivity is rarely uniform. A photon flux hitting different parts of the cathode surface will cause signal fluctuations. In stellar photometry, a Fabry lens system is commonly used that spreads out the incoming light over the whole cathode area for all incident field angles. In addition, the PMT module housing prevents a collinear placement. So, a Fabry lens combination has been integrated into the optical path to reduce signal fluctuations derived from variations in the optical sensitivity of the photo cathode as well as to fill in the gaps between the PMT effective areas. The Fabry lenses, 25mmx16mm, are located close and behind the focal plane of objective lens. The active area of PMTs covering distinct portions of angular field of view (FOV) are somewhat compromised for a benefit of increased SNR by minimizing the background noise. The Fabry lenses and PMT placements conform to the curved focal surface defined by the objective lens. This maximizes the FOV and minimizes the number of lens elements required in the system.

The available space in a 6U CubeSat enclosure does not allow a combination of objective lens that would produce an aberration-free image plane over the full FOV. The collecting lens group is roughly f/1.6, which is extremely fast. The placement of Fabry lenses and PMTs on a curved focal plane trades imaging resolution, within the fan beam, for reduction in off axis aberration. Moreover, due to the required short focal length of the Fabry lens, they are designed using two high index of refraction glasses which reduces the thickness and curvature of the lenses. The ZEMAX optical design program has been used to model and design the lens combination system.

## 1. Introduction

Since the 1957 Soviet space launch of Sputnik, 'Earth's first artificial satellite, debris left in orbit by space missions has degraded Earth's orbital environment and potentially threatens future space programs [2]. The unchecked proliferation of space debris will cause the Earth to be surrounded by a shell of self-propelling debris which poses an increasing threat of collisions and interference with space-based sensors, operating satellites, astronauts, manned spacecraft, and permanent Earth-orbiting space stations. The shell of debris may also hamper or prevent certain space missions.

Space debris is created by rocket bodies, upper stage engines, decommissioned satellites, and fragmentation due to break-ups, collisions, explosions of non-empty tanks etc. [3]. The man-made debris in outer space now form a cloud around the Earth consisting of nonfunctional satellites, spent rocket boosters, nuts, bolts, oxygen tanks and other litter, which increasingly clutters the space surrounding the earth [2]. The number of space debris objects is increasing rapidly, and could reach – in the most populated LEO orbits between 800 km and 1200 km – a run-away point, called Kessler Syndrome [4]: An increasing debris population also increases the collision probability to a value where more debris is created – as a result of collisions – than is removed due to atmospheric drag and re-entry. This scenario is predicted even for the very unlikely case that all future launches stop [3].

An increasing amount of space debris poses a great threat to active satellites [5]. With a velocity of approximately 7 km/s, even collisions with particles of a few millimeters in size can lead to severe damage on satellites. In addition, larger satellites or rocket bodies that do not burn up completely during re-entry impact Earth and may cause damage. [5]. Orbital debris, even smaller than 1 mm, can be fatal to a spacecraft. Therefore, knowledge on micron-size debris should be incorporated in design of spacecraft [6]. The current debris environment at the 10–100-micron level has not been well characterized because measurements have been singular in nature and to specific orbits.

The high kinetic energy of objects orbiting at speeds several times faster than the speediest rifle bullet make the impact of even tiny debris fragments with functioning space equipment potentially catastrophic. The damage caused by orbital debris depends on the velocity and mass of the debris fragments. For debris fragments measuring under 0.01cm, surface pitting and erosion are the primary effects of impact. Over time, the cumulative effect of individual fragments colliding with functioning satellites can pose a significant threat [2]. For debris measuring roughly larger than 0.1 cm, structural damage to satellites becomes an important consideration. For example, a 0.3 cm sphere of aluminum traveling at 10 kilometers per second has about the same kinetic energy as a bowling ball traveling at 100 kilometers per hour (60 mph). In fact, a fragment the size of a salt grain was credited with gouging a centimeter wide pit in the windshield of the space shuttle Challenger in 1983. The chipped outer layer of the triple-panned windshield cost $50,000 to replace. Needless to say, a similar encounter with an astronaut during extravehicular activity could cause human injury or death and abruptly end a space mission [2].

Four known accidental hypervelocity collisions between cataloged objects are known as:

– 1991: Cosmos 1934 struck by piece of mission-related debris
– 1996: CERISE struck by piece of Ariane 1 fragmentation debris
– 2005: U.S. upper stage struck by piece of Chinese upper stage fragmentation debris
– 2009: Collision of Iridium 33 and Cosmos 2251 spacecraft

**1-1. Environment Models**

Modeling techniques can be used to develop near-term engineering, long-term evolutionary, and special purpose models. Regarding the risk assessment, it is desired to develop software tools to permit risk assessments for all NASA space projects including human space flight and robotic. There are two commonly available models of this debris environment, Orbital Debris Engineering Model (ORDEM, NASA) and Meteoroid and Space Debris Terrestrial Environmental Reference (MASTER, ESA) [7]. The current versions of these models have significant discrepancies between them in the millimeter to sub-millimeter population as seen in Figure 1 [8].

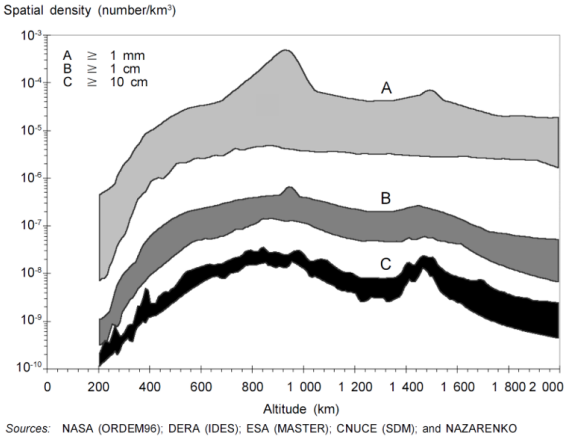


*Figure 1 Model values of space debris spatial density versus orbital altitude. The model estimations disagree up to two orders of Equation 1magnitude [8].*

According to statistical models by ESA an approximate number of 1 million objects larger than 1 centimeter and 130 million space debris particles larger than 1 millimeter exist as shown in Figure 2 [7].

Information is necessary so as to update the models which are based on measurements in the actual environment [6]. The NASA Orbital Debris Program Office (ODPO) has released its latest Orbital Debris Engineering Model, ORDEM 3.0. This newer model encompasses the Earth satellite and debris flux environment from altitudes of low Earth orbit (LEO) through geosynchronous orbit (GEO). Debris sizes of 10 um through 1 m in non-GEO and 10 cm through 1 m in GEO are modeled for the period from 2010 through 2035 [9].

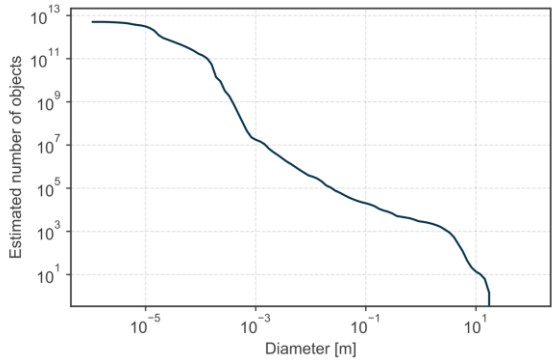


*Figure 2. Estimated number of space debris objects as function of the object size in Earth orbit [7].*

**1-2. Previous Measurements**

Space-based measurements in general have the advantage of higher resolution because of the smaller distance between the observer and the object. Radar measurements from the surface suffer from the disturbing effects of the atmosphere (extinction and absorption of electromagnetic signals). However, the cost of a space-based measurement tool is in general higher than the cost of ground-based systems, and careful cost-performance trade-offs are needed [8]. During wide field imaging, astronomers now routinely observe an increasing number of "trails" per photographic "plate" caused by space debris. These trails degrade the quality of the photometric observation. Space debris trailing will entirely negate a photometric observation when debris cross the narrow photometric field.

Remote sensing of space debris from ground-based measurements generally falls into two categories: radar measurements and optical measurements [8]. Typically, radar measurements have been used for space debris in low Earth orbit (LEO), while optical measurements have been used for high Earth orbit (HEO) [8]. Debris can be detected by a telescope when the debris object is sunlit while the sky background is dark. For objects in LEO, this period is limited to an hour or two just after sunset or before sunrise. However, for objects in HEO, such as those in geosynchronous orbit, observations can often be continued during the entire night [8]. The capability of these telescopes is limited to detection of objects of 1 m at geosynchronous altitudes, corresponding to a limiting stellar magnitude of 16.

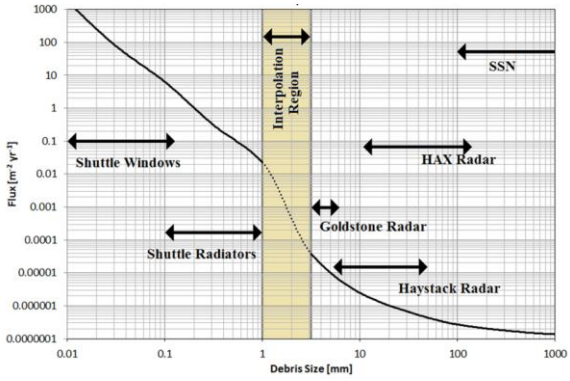


*Figure 3. Total flux of space debris at the typical ISS orbit (400km. 51.6º) versus the debris size in millimeter. The interpolation region in yellow strip is associated with the modeling estimation as no sufficient measurements are still available [9].*

Since 1971, regular measurements of submillimeter-sized meteoroid and debris particles have been carried out on the Russian space stations Salyut 1, 2, 3, 4, 6 and 7 and Mir. The measurements have been carried out by capacitive sensors with an overall exposed area of about 3 $m^2$, as well as by changeable returned cassettes with an exposed area of about 0.1 $m^2$ each. In January 1998, during the Space Shuttle mission, eight sections of solar panels from the space

station Mir, with an overall area of about 10 $m^2$ and an exposure time of about 10 years, were returned to Earth for further investigation [8].

The NASA Orbital Debris Program Office has developed the Orbital Debris Engineering Model (ORDEM) primarily as a tool for spacecraft designers and other users to understand the long-term risk of collisions with orbital debris. The newest version, ORDEM 3.1, incorporates the latest and highest fidelity datasets available to build and validate representative orbital debris populations encompassing low Earth orbit (LEO) to geosynchronous orbit (GEO) altitudes for the years 2016-2050 [10]. ORDEM 3.1 models fluxes for object sizes > 10 µm within or transiting LEO and > 10 cm in GEO [10]. The deterministic portion of the populations in ORDEM 3.1 is based on the U.S. Space Surveillance Network (SSN) catalog, which provides coverage down to approximately 10 cm in LEO and 1 m in GEO Observational datasets from radar and optical sources provide a foundation from which the model populations are statistically extrapolated to smaller sizes and orbit regions that are not well-covered by the SSN catalog, yet may pose the greatest threat to operational spacecraft as shown in Figure 3 [10].

Objects in LEO ranging from approximately 5 mm to 10 cm are modeled using observational data from ground-based radar, namely the Haystack Ultrawideband Satellite Imaging Radar (HUSIR – formerly known as Haystack). The LEO population smaller than approximately 3 mm in size is characterized based on a reanalysis of in situ data from impacts to the windows and radiators of the U.S. Space Transportation System orbiter vehicle, i.e., the Space Shuttle [10]. Data from impacts on the Hubble Space Telescope are also used to validate the sub-millimeter model populations in LEO. Debris in GEO with sizes ranging from 10 cm to 1 m is modeled using optical measurement data from the Michigan Orbital DEbris Survey Telescope (MODEST) [10].

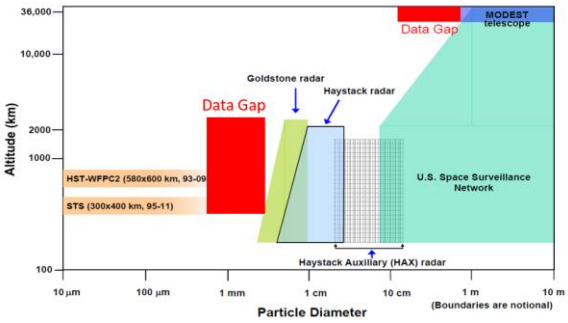


*Figure 4. Orbital debris measurement coverage for varying altitudes versus debris diameter [1]. Red area represents the measurement data gap. The desired lidar sensor would address this data gap by characterizing small debris (100µm –5mm), in situ at LEO orbits and without tactile contact.*

## 2. Lidar Sensor for Space Debris Characterization: System Design

To optimize the transmit laser power and considering the debris particles will impact at limited angles, the transmit laser is shaped into a fan beam. Modeling tools are used to create a link budget, for light scattering and return, which is used to evaluate sensor performance and inform modifications to the design. To achieve a wide field of view, the sensor-receive optics must incorporate fast optics (low F/#) or wide-angle lenses [11]. In applications with lasers, the transmit-optics, the telescope, are often referred to as beam expanders, since it adapts the small laser beam diameter to the mission requirements [12]. Of the two well-known types of telescopes, the Keplerian and the Galilean, the latter, which use a positive-negative combination of optical elements, is preferred in laser applications because it avoids an intermediate focus and is shorter. A functional schematic of the debris Lidar sensor is shown in Figure 5.

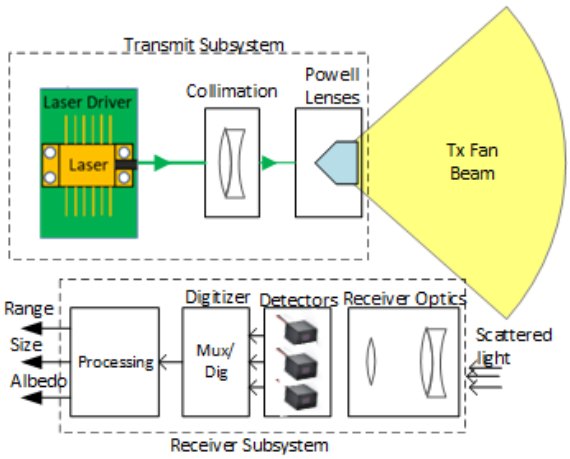


*Figure 5. General architecture of specific Lidar sensor designed for characterizing space debris. The receiver will make a low-resolution imaging by dividing the entire FOV within the transmit fan beam into three regions. Each region is associated with a single large PMT detector.*

### 2-1. Transmitter System

Starting from the optical properties of laser beams, the requirements of optical systems for manipulating laser radiation in industrial applications are derived. Each wavelength range is associated with specific design challenges. Reflective systems are used widely at the longer wavelength, but some designs suffer from coma. The 1.06 um radiation from the Nd: YAG laser can make use of many well developed optical means for handling visible light [12]. The analogy with noncoherent radiation may be extended to the generation of an image, which is the formation of a diffraction pattern from a converging phase front at some point in space, and which may be simulated by calculation of the (Huygens) diffraction integral [12]. While incoherent beams are usually limited by hard aperture stops to well-defined beam widths, the definition of that quantity for laser beams is much less obvious [12].
In this design, the laser energy is spread using a pair of Powell lenses with angles θx and θy (see Figure 6). Here, the x-dimension axis is the larger spread, of full angle θx, and the y- unit vector is parallel to the in-track velocity of the satellite.

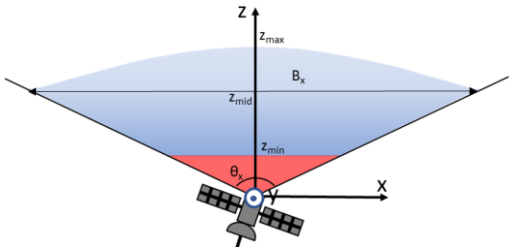


*Figure 6. Transmit laser: the laser beam is shaped into a thin fan using a pair of Powell lenses.*

A Powell lens converts the initial Gaussian distribution of energy into a nearly flat-top energy distribution to form a "line" beam or "rectangle" beam in the case of two lenses. Thus, the overlap loss is:

$$L_{olp} = \frac{\pi r_T^2}{B_x B_y}$$

$B_x$ and $B_y$ are the widths of the beam for a particle that intercepts the primary fan axis at $z_T$ ($r_T = \|(x, y, z)\|_2$).

### 2-2. Receiver System

The beam spread in the y direction, with angle $\theta_y$, along with laser pulse repetition rate enables the capture of two or more scattering returns from an intercepted piece of orbital debris that manages to cross the laser-net. The multiple returns are used to determine the relative velocity. The area defined as $z < z_{min}$ does not meet the condition for multiple returns from single particle. Returns from this distance range are excluded.

To assess whether a particle detection has been made given a specified optical cross section and diameter, the signal to noise (SNR) of the spatially determined returns is calculated and compared with a threshold value. We use a threshold of $SNR_{min}$ = 10 to meet the detection need for quantitative debris size estimation, and a $SNR_{min}$ = 3 for simple detection and counting purposes. Using this radiometric model, parameters including $\theta x$, $\theta y$, $z_{min}$, P, $f_R$, and $\tau_p$ (the laser pulse duration) can be optimized separately or together for debris of varying optical cross sections.
Since the small particle debris models show a large discrepancy in sub-cm size regime and such large differences make assessment of satellite reliability difficult and to evaluate whether a space-based CubeSat-hosted lidar could create an effective "collection area" of such size as to detect enough small particles to improve the environment models (ORDEM and MASTER), a simulation was performed examining several potential orbits and possible lidar configurations. Figure 7 shows the expected flux for the >1 mm particles in units of number of particles per unit area per year, and exhibits the basic problem described earlier: there is a large discrepancy between environmental models (an order of magnitude difference or more).

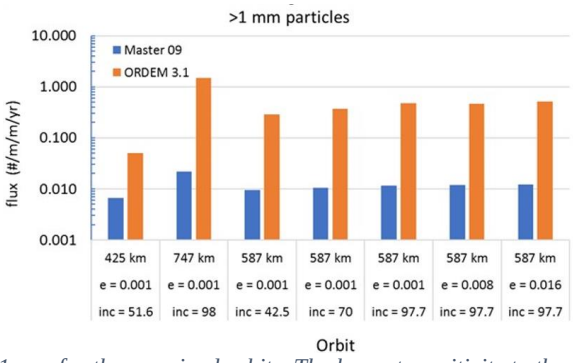


*Figure 7. The flux if particles >1-mm for the examined orbits. The largest sensitivity to the results is the mean altitude of the orbit.*

**2-3. System Parameters**

Higher inclination orbits would detect more particle flux than lower inclinations, and orbits with higher apogees (for a given mean altitude) saw more particles than purely circular orbits. However, the most significant trend is that orbits that are higher in mean altitude (in this case 747 km) yielded more potential particles than the lower orbits (although historically, the lower orbits are more likely to be available for CubeSat secondary payload deployment and are also more likely to meet the 25-year decay requirement).
The laser power range considered ranges from 5 to 10 W with the laser repetition rate ranging from 250–600 kHz. The effective collection area for the smaller particles at 0.1 mm size is much smaller than the area for the 1 mm particles, but there are also more particles of the 0.1 mm size which offsets the decreased area.
One point to consider: if the lidar fan beam is fixed perpendicular to the bow direction (i.e., the CubeSat is attitude controlled), then the detector will "see" all the passing orbital debris particles since most particles are coming directly at the detector. If CubeSat is not attitude controlled but instead is tumbling, then the effective collection area is halved. While it is unlikely that any 1 cm particles will be detected, the Lidar sensor should observe many 0.1 mm particles (40-465 particles per year) and will see up to 57 1-mm class particles per year (numbers are based on the available models).
Increasing the laser power also increases the area of detectability, as shown in Figure 8. However, for large pulse energies, the slope is considerably less than one, which means that increasing laser power is not necessarily the most effective way of increasing collection area. Leaving all other parameters of the detector unchanged, two 5W laser detectors will yield greater collecting area than a single 10W laser detector.

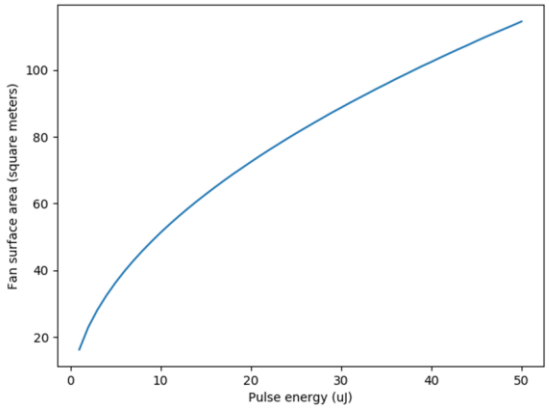


*Figure 8. General scaling of fan area with input pulse energy for an unspecified scenario.*

A change in the laser repetition rate does not change the predicted collecting area if the fan beam angles can also be appropriately adjusted. So, the lidar fan beam characteristics used in the model are adjusted such that two observations of a particle are guaranteed for a relative velocity of 14–15 km/s. On average the minimum passage time through the detection-fan is ~3.6 msec. This information could then be used to a generate an approach vector (and hence orbit) for the particle. In summary, a lidar with this configuration would yield not only the flux magnitude at a given altitude, but the flux direction as well. A caveat must be acknowledged that these estimated particle detection counts assume that the two available environment models approximately represent the small particle environment.

There are two sources of particles that a lidar detector could observe: orbital debris and micrometeoroids. On the average, micrometeoroid flux is much lower than the flux from orbital debris, so the detector is unlikely to see many micrometeoroid particles (unless during a meteoroid shower), but if it does, the micrometeoroid approach vectors are very different from what orbital debris particles create. Orbital debris will approach a satellite at relative speeds up to ~15 km/sec and for the most part head-on with respect to the satellite's motion. The micrometeoroids, since they are in heliocentric orbits and so are on hyperbolic trajectories relative to the Earth, will have average speeds exceeding 20 km/sec and much steeper approach angles. Figure 9 shows histogram plots of the velocity and direction for the high density (iron and stony) and low density (fluffy) micrometeoroids along with the expected range of orbital debris particles. As a result of these populations being so different in their encounter characteristics, micrometeoroid and orbital debris particles can be uniquely separated in post-processing.

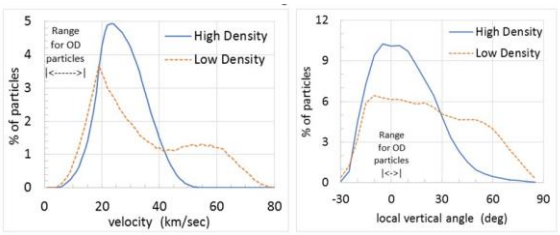


*Figure 9. Micrometeoroid velocity and approach angle histogram. The orbital debris and micrometeoroid populations show different characteristics indicating their signals can be separated.*

## 3. Optical design of Receiver

It was shown in Figure 5 that the receiver part of the Lidar sensor consists of a. optics, b. detectors, c. readout board and d. pot-processing unit. The optical subsystem of receiver includes the optics and detectors. These two parts are mutually dependent on one another. Here, we are discussing the selection of these tow optical subsystems for the desired lidar sensor.

### 2-4. Detector

There are two candidate detectors: Avalanche Photodiode (APD), and Photo-Multiplier Tubes (PMT). Each category is here explained.

**APD**: An APD is like a PIN photodiode but provides internal photo-electronic signal gain. An APD will normally be operating in one of two noise-limited detection regimes; either detector noise limited at low power levels, or photon shot noise limited at higher powers. Sensitivity at low light levels will be limited by the shot noise and the APD's leakage current. APD can offer a combination of high speed and high sensitivity unmatched by PIN detectors, and

quantum efficiencies at >400 nm unmatched by PMTs. Sensitivity at low light levels will be limited by the shot noise and the APD's leakage current. Shot noise derives from the random statistical Poisson fluctuations of the dark of dark current, $I_D$ (or signal current). Dark current shot noise is normally given by:

$$i_n(shot) = (2.q.B.I_D)^{1/2}$$

Where B and q represent bandwidth and electron charge respectively. In APD, the current is composed of the bulk leakage current $I_{DB}$ and the surface leakage current $I_{DS}$ in which the bulk leakage current is multiplied by the gain $M$. The avalanche process statistics generate current fluctuations such that APD performance is degraded by an excess noise factor $F$. Accordingly, the total noise component for an APD detector in dark condition can be described as:

$$i_n = \sqrt{2.q.B.(I_{DS} + I_{DB}.M^2.F)}$$

If the APD detector is illuminated with light power $P_S$, the total noise of APD at illuminated condition increases as follows:

$$i_n = \sqrt{2.q.B.(I_{DS} + (I_{DB}.M^2 + R_o(\lambda).M^2.P_s).F)}$$

So, at higher signal light levels, the detector transitions to the photon shot noise limited regime. In an APD, there are two charge carriers, electrons, and holes. Both can trigger the impact ionization to generate new electron-hole pairs with impact ionization ratio of $k_{eff}$. Then, the excess noise factor $F$ can be defined as:

$$F = k_{eff}.M + (1 - k_{eff})(2 - \frac{1}{M})$$

In the absence of other noise sources, an APD therefore provides a signal-to-noise ratio (SNR) which is $\sqrt{F}$ worse than a PIN detector with the same quantum efficiency.

**PMT**: In a PMT, photons are absorbed by photocathode to produce an electron which is then amplified by a series of dynodes. Currently, PMTs are the most successful weak signal detectors given the high gain (greater than $10^6$) it can achieve under constant bias (linear mode) operation. But PMTs are large and fragile objects difficult to package safely. This limits its applications in many frontier domains (see Figure 10). However, as with the photo detector for weak optical signal, solid state device still cannot replace the PMT thoroughly.

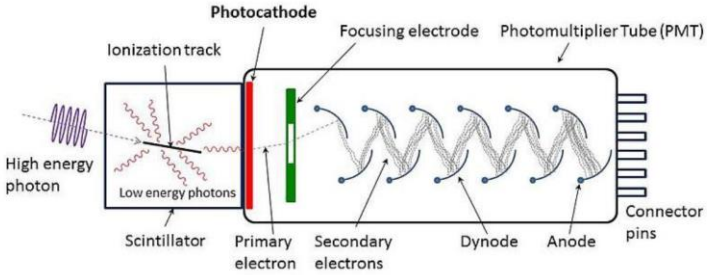


*Figure 10. Photomultiplier tube: constructed from a glass envelope with a high vacuum inside, which houses a photocathode, several dynodes, and an anode. Photons produce electrons at the photocathode (photoelectric effect) and multiplied by the process of secondary emission through dynode until get the anode [13].*

Multi-alkaline photocathode e.g., Na-K-Cs can sense from the UV to near IR with a quantum efficiency $\eta$ of about 20% at 530nm. Though, there is no photocathode with good efficiency for lambda greater than 1 micron. There are photocathodes of Ag-O-Cs with $\eta$<0.1 that can work for the Nd:YAG laser wavelength at 1060 nm. For these PMTs, the gain (number of electrons at anode to number of photoelectrons from cathode) is still very high to compensate for the low quantum efficiency.

In this Lidar design, the receiver optic should have a wide angle FOV. To account for this wide FOV, and with the APD sensor option would necessitate the use of an array with a large number of detectors. These devices are high cost with more complexity in the read-out board. Since the required Lidar sensor doesn't need a high *angular resolution*, we can use PMT detectors to benefit from its specific properties: a. large active area or photocathode considerably reduces the number of detectors required, b. lower noise at high gain compared to APD detectors, c. simpler read-out electronic board without front-end analog amplifiers by using a few PMT detectors.

**2-5. Receiver Optics**

The Receive optics is responsible among others for, a) increasing the photon capture at the photocathode through a wide aperture, b) minimizing unwanted noises from background and sun-scattered lights by filtering, and c) managing the division of the FOV among the multiple (three) detectors. In contrast, the Receive optics is driven by the need to a) maximize sensitivity, b) minimize weight, and c) limit the overall size to something close to the dimensions of a 6U CubeSat. In addition, it should provide the widest fan beam angle. Overall, the design is based on using three selected PMT detectors, though it can be scaled to more detectors and a wider FOV.

In pursuit of maximum sensitivity, PMTs with large active area (Hamamatsu, H15460) were selected as the detectors with an objective lens with a maximum aperture consistent with a 6U enclosure, that being 90 mm in diameter. Maximizing sensitivity with a wide angle FOV drove the design to a fast wide angle lens configuration. Several choices of aperture size and f/number were investigated and in order to keep aberrations under control while avoiding excessive complexity, we converged on an f/1.6 objective lens with a 90 mm diameter aperture and 144 mm focal length. This system is a photon counting rather than imaging system, and aberration might seem not to be an issue. However, the aberration here leads to a transition region between adjacent detectors that would complicate the detection of weak return signals bouncing off the tiny debris particles. So, aberration not only divide very few returning photons between two adjacent detectors (lowering the minim detectable particle size), but also have some complications on the post processing stage to determine the sub-FOV region in which scattering particle is located.

Commercially-Off-The-Shelf (COTS) wide angle lens designs typically make use of a large number of lens elements with a significantly oversized first lens element to obtain well corrected images, with a flat focal plane and with minimal vignetting. This is not compatible with a system constrained by a volume close to that of a 6U CubeSat enclosure. In addition, such a lens would be unacceptably heavy for a CubeSat flight system. Taking all of this into consideration, as well as the fact this LIDAR receiver does not require a small iFOV (angular resolution is not priority), we chose to limit the objective lens to a three-element design, accepting a small amount of vignetting and allowing a curved focal plane. The curved focal plane, in fact, is advantageous as it facilitates the mechanical configuration of the PMT modules. The objective lens has 10 µm diameter spots with a small amount of residual spherical aberration. Since the system is detecting monochromatic laser light, only minor effort was devoted to controlling chromatic aberration.

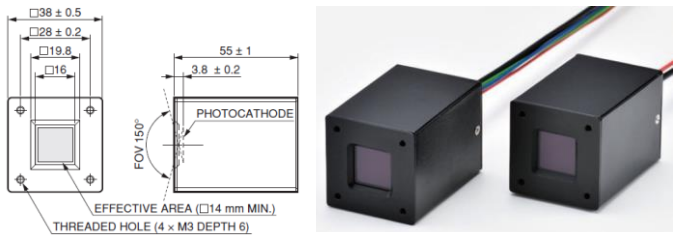


*Figure 11. PMT modules H15460 from Hamamatsu were used in the optical design. They included GaAsP photocathodes and large effective area of* $14 \times 14$ *mm.*

The PMTs chosen for the receiver have $14 \times 14$ mm photocathodes in an integrated module that is $38 \times 38$ mm in size on the face exposing the photocathode (see Figure 12). The simplest approach for the PMTs would be to place them at the curved focal plane. This requires simply placing the PMTs at the curved focal plane, oriented tangent to the focal plane curvature. Such a configuration would consist of a receiver with three square fields of view with large dead spaces in between (due to the PMT housing), and not the desired fan beam. Thus, to illuminate the PMTs, Fabry lens sets are placed at the focal plane of the objective lens.

**Fabry Lens:** A simple Fabry lens is a lens element at or near the focal plane of an imaging system that images the aperture onto the surface of a detector [14]. For every field angle incident upon the Fabry lens, the light from the field angle is distributed over the image of the aperture on the active surface of the detector (see Figure 12). If Fabry lenses are designed correctly, every field angle illuminates the detector in the same way, making the detector output independent of field angle incident on the Fabry lens. This is the way PMTs were first used for astronomical aperture photometry in the early days of PMTs as the response of PMTs are not uniform over the extent of the photocathode [15-17]. In addition to mitigating the non-uniformity of the photocathode sensitivity, a Fabry lens at the focal plane acts as a field stop that determines the total field of view for the PMT it illuminates. A Fabry lens can also be placed behind an actual mechanical field stop [pinhole, etc.] and image the aperture on the detector [17]. This approach is not acceptable for our LIDAR receiver as it would also create gaps and regions of reduced response in the transition from one PMT to the next.

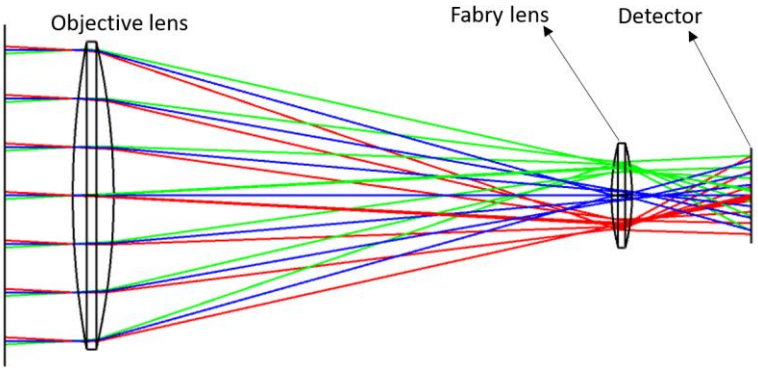


*Figure 12. Fabry lens: a simple converging lens is inserted into the optical trail just before the detector in a way that keeps all the ray cones onto the detector area.*

Because the objective lens is significantly wide angle, with a relative fast f-number, the rays propagating through the system largely pass through the lens elements at significant angles. The result is that as single element Fabry lens will not adequately do the required task. In addition to residual aberrations and impractical sizes, one may find some field angle lead to total internal reflections in the Fabry lens, and so we make use of a compound lens set to act as the Fabry lens to eliminate these problems. We will refer to this as a Fabry lens set in the following (see Figure 14).

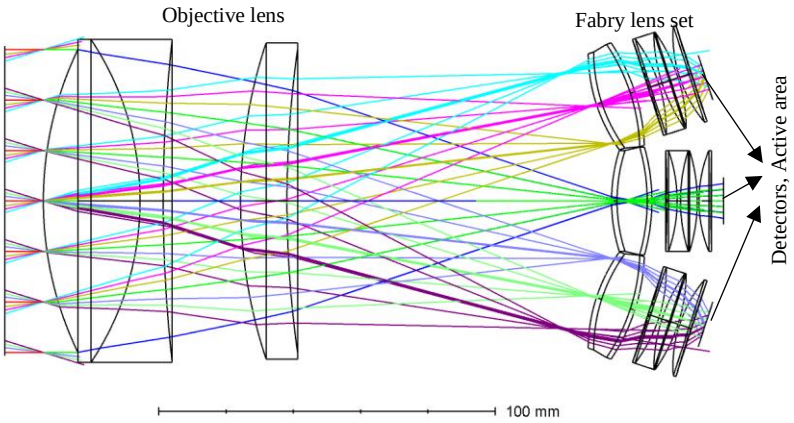


*Figure 13. Overall architecture of the receive optical system. The optics include two parts: collective lens and Fabry lens set and optical trials ends up in photocathodes for on- and off-axis optical paths.*

Each PMT has a Fabry lens set consisting of five lens elements. The first lens element is rectangular in shape and defines the FOV for the associated PMT. The remaining lens elements are round. The last lens element is plano-convex, with the PMT housing lying close behind it. In between the first and last lens elements is a triplet element. The Fabry lens sets illuminate the PMTs with14 mm diameter spots. These spots are not perfect images of the aperture, but close enough to meet the design goals of the LIDAR receiver. A perfect imaging of aperture onto the photocathode area would require a more complex design that is not required at this phase (see Figure 14).
In the current configuration Figure 15Figure 14, one Fabry lens set and PMT lies on axis, while two others are oriented to conform to the curvature of the focal plane. These subassemblies are in contact at the edges of the front lens elements. Light falling on or near the junction of the three rectangular lens elements [within the size of the image spots] will end up being split between two adjacent Fabry lens sets. In this design the receiver FOV is essentially $1 \times 3$ pixels with each pixel approximately $6 \times 11$ degrees, with vignetting near the edges of only a few percent.

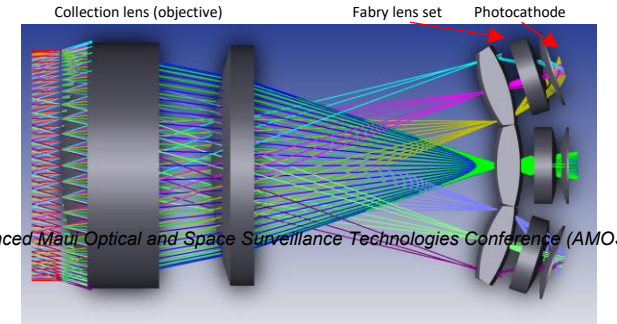

*Figure 14. Receiver optical system designed ad optimized using Optic Studio (ZEMAX) 2024R1.*

The receiver was optimized for sources at infinity (see Figure 15). In practice the intent is to receive returns from debris within 0.5 m of the receiver ($z_{min}$). As debris particles are located closer to the objective lens at a finite object distance the image distance increases with the focal plane farther from the objective. In effect, this puts the Fabry lens sets somewhat in front of the focal plane for nearby debris. This makes them less effective in imaging the aperture on the PMTs and reduces the spot size on the photocathode. To the extent the PMTs may not have perfectly uniform spatial response on the scale of the smaller spot size this may result in some variation in response with field angle, particularly as a debris target moves through the field of view and potentially changes position on the photocathode. Since the LIDAR is not meant to be a precision radiometric sensor, we accept this residual signal variation giving priority to getting a detection from debris close to the system.

We examined whether there was any value in optimizing the Fabry lens sets with respect to the angle at which they are used off axis, at an associated increased cost. It turns out that by introducing small translations and decenters of some of the elements within the Fabry lens set and PMT design we can compensate for differences in off axis image quality. The main issue we are trying to control with this is eliminating vignetting on the off-axis photocathodes which we can do well.

In principle our approach could be extended to using five PMTs. We expect, however, a set of PMTs even farther off axis will probably require Fabry lens sets optimized specifically for those greater field angles. The receiver is looking for returns from a monochromatic visible laser, so limited effort was put into achromatizing the system. In addition, a filter to isolate the laser radiation from ambient background is needed.

**Optical filter selection:** The PMTs, of course, are broadband detectors. Thus, to isolate the laser light from ambient visible background over the full responses of the PMTs a laser line filter is needed. The filter selection is implemented considering two constraints: First, the filter band is constrained by the large angle of incidences, secondly, there is a limited space through the optical system The receive beam is not collimated at any point within the receiver optics. So, being a wide-angle system with large ray angles propagating through the system, there will be significant changes to the filter band center and edges from a nominal filter design considering the dependencies on the angle of incidence. This prevents use of a very narrow band filter. We expect filters of 50-100 nm bandwidth will be required to overcome the bandwidth shift due to the ray angles. Filters of this width will be more accommodating to changes in the bandpass while still allowing the laser light to pass. Second, there are few places in the design where there is sufficient space to place a filter without degrading the image quality. We are basically limited to 1 mm thick filters, at best. A compromise will be made to determine the best location of the filter. In part this will depend on the coating manufacturers.

One choice for filter location is to place a $16 \times 16$ mm square 1 mm thick filter directly at the front surface of the phototubes. The second choice under consideration is to coat the plano surface of the last element in the Fabry lens sets with the filter coating. The advantage of this is that it will have no impact on optical performance. A drawback is that if one wanted to change the filtration that lens element would have to be stripped and recoated. The final choice may end up largely determined by the manufacturing quality.

## 4. Simulation Results

The optical design was implemented and optimized in the Optic Studio ZEMAX 2024R1. The design configuration consists of two set of lens combinations: a single collecting lens combination with wide aperture (90mm) that collect the scattered light and feeds the next optical subsystem, a Fabry lens combination per detector (see Figure 15). The designed configuration was adjusted to cover an FOV of $10.5° \times 10.5°$ per detector. Figure 16 demonstrate the binocular FOV for each detector. The leftmost or first lens of the Fabry lens combination is cut into appropriate square shape to match the photocathode geometry. However, the rest of the lenses in the combination kept in circular form.

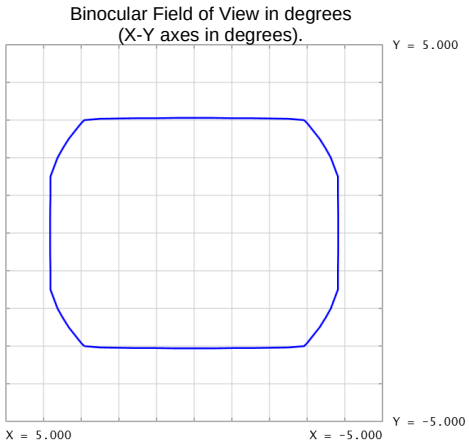


*Figure 15. Binocular FOV for X-Y axes in degrees with sharp unvignetted region of 10.5º per detector. The first lens of the Fabry lens combination is cut into square form to match the photocathode shape.*

The specific design of Fabry lens combination is different from conventional Fabry lenses used for astronomical aperture photometry. The complementing lens following the initial Fabry lens in the combination releases the geometrical constraints on the primary Fabry lens. Given this new feature, we are able to push the primary Fabry lens closer to the focal plane of the objective lens. So, the aberration or vignetting region around the boundary of the primary Fabry lens is minimized (if not completely removed due to diameter of the Fabry lens). All that enabled to come up with a very sharp vignetting plot as shown in Figure 17.

On the other hand, the Fabry lens combination provide an appropriate size of the image spot per detector in a way that keeps the image within the active area of $14 \times 14mm$ per detector. This requirement is relaxed a little bit at the boundary of field of view as the focal spots do not hold exactly on the primary Fabry lens's surface. Figure 18 demonstrates the footprint of aperture across a field of 10 degrees. This compromise is acceptable to have a simpler Fabry lens combination and large active area.

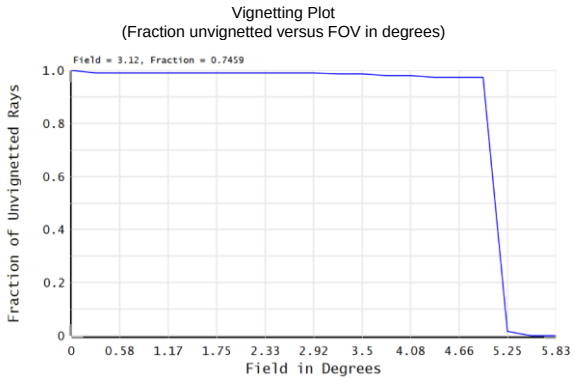


*Figure 16. Vignetting plot per detector: Fraction of unvignetted rays versus the field angle. The Fabry lens combination results in a very sharp vignetting plot. The narrow vignetting transition region makes a one-to-one association between the detector and FOV subregion.*

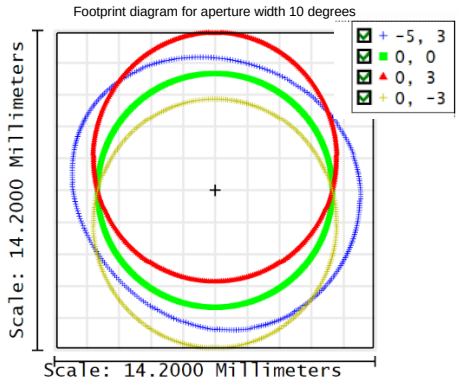


*Figure 17. Footprint diagram for aperture width of 10 degrees per detector for different ray cones within the aperture. Given the 14x14mm photocathodes, the design can concentrate the ray cones onto the photocathode across the FOV with only minor vignetting near the edge of the fan beam.*

In summary, the optical design of the Lidar receiver is completed on the basis of removing aberration effects (vignetting) by restricting the rays across the photocathode. A Fabry lens combination per detector enabled tackling the aberration effects as well minimizing the vignetting region between adjacent photocathodes. The overall design is compacted to a front surface to detector length of 144mm with $90mm$ of aperture consistent with CubeSat. The optical modeling shows a sharp unvingetted region 10.5° per detector, $\pm 0.35°$vignetting per detector, and no blind angle with total FOV of 39°. All the optical components are fabricated from standard optical glasses. The design is simply scalable to larger FOVs by using 5 PMTs as well.

## 5. References


1. Hamilton, J., et al. *Development of the space debris sensor*. in *European Conference on Space Debris*. 2017.
2. Atney-Yurdin, I., *Space Debris Legal Research Guide.* Pace YB Int'l L., 1991. **3**: p. 167.
3. Kirchner, G., et al., *Laser measurements to space debris from Graz SLR station.* Advances in Space Research, 2013. **51**(1): p. 21-24.
4. Kessler, D.J., et al., *The kessler syndrome: implications to future space operations.* Advances in the Astronautical Sciences, 2010. **137**(8): p. 2010.
5. Steindorfer, M., et al. *Space debris science at the satellite laser ranging station Graz*. in *2017 IEEE International Conference on Environment and Electrical Engineering and 2017 IEEE Industrial and Commercial Power Systems Europe (EEEIC/I&CPS Europe)*. 2017. IEEE.
6. Hanada, T., *Orbital debris modeling and applications at Kyushu University.* Procedia Engineering, 2013. **67**: p. 404-411.
7. Office, E.S.D., *ESA'S ANNUAL SPACE ENVIRONMENT REPORT*. 2024.
8. United Nations, *Technical report on space debris*, in *New York, USA, ISBN*. 1999, Committee on peaceful uses of outer space. p. 92-1.
9. Krisko, P.H. *The new NASA orbital debris engineering model ORDEM 3.0*. in *AIAA/AAS Astrodynamics Specialist Conference*. 2014.
10. Matney, M., et al. *The NASA orbital debris engineering model 3.1: development, verification, and validation*. in *International Orbital Debris Conference (IOC)*. 2019.
11. Curatu, G., *Analysis and design of wide-angle foveated optical systems*. 2009: University of Central Florida.
12. Beckmann, L. and D. Ehrlichmann, *Optical systems for high-power laser applications: principles and design aspects.* Optical and quantum electronics, 1995. **27**: p. 1407-1425.
13. Göhler, A. *Detectors for microscopy-CCDs, sCMOS, APDs and PMTs*. 2015; Available from: https://downloads.micron.ox.ac.uk/lectures/micron_course_2015/Lecture_10_cameras.pdf.

14. Wall, J., *The practical application of transfer and Fabry lenses.* Journal of the British Astronomical Association, vol. 108, no. 6, p. 326-329, 1998. **108**: p. 326-329.
15. Connes, J. and P. Connes, *Near-infrared planetary spectra by Fourier spectroscopy. I. Instruments and results.* JOSA, 1966. **56**(7): p. 896-910.
16. A'Hearn, M.F., *Comments on: Fabry Lens.* Applied Optics, 1972. **11**(8): p. 1874-1874.
17. Michlovic, J. and F. Cooke, *Fabry Lens.* Applied Optics, 1972. **11**(2): p. 490-491.